Implicit Algorithm for Threshold Stream Power Incision Model

Journal Article

Author(s):
Braun, Jean; Deal, Eric

Correspondence to:

J. Braun,
jbraun@gfz-potsdam.de

Implicit Algorithm for Threshold Stream Power Incision Model

Jean Braun[1,2] and **Eric Deal[3]**

[1]Helmholtz Centre Potsdam, GFZ German Research Centre for Geosciences, Potsdam, Germany, [2]Institute of Earth and Environmental Sciences, University of Potsdam, Potsdam, Germany, [3]Earth Surface Dynamics, Geology Institute, ETH-Zürich, Zürich, Switzerland

Abstract We present an $O(n)$ complexity and implicit algorithm for the two-dimensional solution of the stream power incision model (SPIM) enriched by a discharge threshold term and taking into account variability in rainfall and thus discharge. The algorithm is based on the formulation developed by Deal et al. (2018, https://doi.org/10.1002/2017jf004393) and the generalization of the FastScape algorithm (Braun & Willett, 2013, https://doi.org/10.1016/j.geomorph.2012.10.008) where the slope is approximated by first-order accurate finite difference. We consider a variety of discharge thresholds that vary in their dependence on channel slope. The algorithm requires finding the root of a non-linear equation using a Newton-Raphson iterative scheme. We show that the convergence of this scheme is unconditional, except for a narrow range of model parameters where the threshold increases with the slope and for low discharge variability. We also show that the rate of convergence of the iterative scheme is directly proportional to the slope exponent n in the SPIM. We compare the algorithm to analytical solutions and to numerical solutions obtained using a higher-order finite difference scheme. We show that the accuracy of the FastScape algorithm and its generalization presented here is comparable to other schemes for values of $n > 1$. We also confirm that the FastScape algorithm and its generalization to variable discharge + threshold conditions does not need to satisfy the *CFL* condition and provides an accurate solution for both small and very long time steps. We finally use the new algorithm to quantify how the existence of an erosional threshold strongly affects the length of the post-orogenic decay of mountain belts.

Plain Language Summary The stream power incision model is a computational model that is widely accepted to represent the rate of incision by rivers into bedrock. Recent work has shown how discharge daily variability influences the rate of incision. This demonstration has only been done at the local level, that is, at a given point in a landscape. Here we present an algorithm that allows to implement the effect of discharge variability in a two-dimensional landscape evolution model. In most practical situations, our algorithm is very efficient as the computation time it requires is directly proportional to the number of nodes used to discretize a synthetic landscape and it is also very stable as it allows for very large time steps. We show under which exact conditions this statement is true. We also use the model to demonstrate the importance of discharge variability on the longevity of mountain belts.

1. Introduction

There has been much debate about the links between erosion and climate, in particular about how rainfall intensity and thus river discharge affects erosional efficiency (DiBiase & Whipple, 2011; Scherler et al., 2017a; Snyder et al., 2003; von Blanckenburg, 2006). In its simplest form, the widely used stream power incision model (SPIM) states that the erosion rate of a river should be proportional to river discharge to some poorly known power (Whipple & Tucker, 1999). Recent work has shown that rainfall and thus discharge variability are important too when erosion only takes place above a certain discharge threshold (Deal et al., 2018; Lague et al., 2005; Tucker & Bras, 2000). Consequently, much work has been devoted to assess the importance of such thresholds (Scherler et al., 2017b), to characterize them and, in particular, to determine whether they depend on channel slope or not (Lamb et al., 2008).

Recently, Deal et al. (2018) have proposed an improved version of the SPIM that takes into account the existence of an erosional threshold in determining erosional efficiency under variable rainfall/discharge conditions. Here, we propose a new numerical implementation of this improved SPIM, which we will call TS-SPIM, that is of

complexity O(n) and implicit in time and therefore very efficient and unconditionally stable. Our approach is an extension of the FastScape algorithm developed by Braun and Willett (2013) for the SPIM.

We will present the new method and its implementation for a range of threshold definitions, that is, proportional, inversely proportional or not proportional to channel slope. The method relies on the solution of a non-linear equation by Newton-Raphson iterations. We determine, for a wide range of thresholds, the conditions and rate of convergence of this scheme. Finally, we compare the accuracy of the method with higher-order but slower and less stable numerical schemes.

2. The TS-SPIM

We start from the following expression derived in Deal et al. (2018) (their Equation 25) for the long-term or time integrated erosion rate, $< E >$:

$$< E > = \mu_\epsilon K \mu^m A^m S^n - \lambda_\epsilon \Psi \tag{1}$$

where K is a constant, μ is specific mean daily streamflow, A is upstream drainage area, S is slope and Ψ is the threshold for erosion ($\Psi = k_e \tau_c^a$, where τ_c is the critical shear stress for erosion to occur, k_e is an erosional constant and $a = 3n/2$ is an exponent reflecting the dominant erosion mechanism). μ_ϵ is the nonlinear average of daily streamflow above the threshold and λ_ϵ is the probability of streamflow exceeding the threshold.

Deal et al. (2018) have derived expressions for μ_ϵ and λ_ϵ based on a physically realistic model of basin hydrology that describes daily streamflow variability with a parameter b, representing the non-linearity of streamflow recession and, consequently, the heaviness of the tail of the distribution of daily streamflow. We will consider here only three cases corresponding to $b = 1$ (streamflow distribution is a gamma distribution), $b = 1.5$ and $b = 2$ (streamflow distribution is an inverse gamma distribution). These expressions are (Deal et al., 2018):

$$\mu_\epsilon = \frac{\Gamma(1/\nu + \gamma)}{\Gamma(1/\nu)\nu^{-\gamma}} \Gamma(1/\nu + \gamma, q_{c*}/\nu)$$
$$\lambda_\epsilon = \Gamma(1/\nu, q_{c*}/\nu) \tag{2}$$

for $b = 1$,:

$$\mu_\epsilon = \frac{K_{(2\gamma-1)}(4/\nu)}{K_{-1}(4/\nu)} \Gamma_g(2\gamma - 1, 2q_{c*}/\nu; 4/\nu^2)$$
$$\lambda_\epsilon = \Gamma_g(-1, 2q_{c*}/\nu; 4/\nu^2) \tag{3}$$

for $b = 1.5$ and:

$$\mu_\epsilon = \frac{\Gamma(1/\nu + 1 - \gamma)}{\Gamma(1/\nu)\nu^{\gamma-1}} \gamma(1/\nu + 1 - \gamma, 1/\nu q_{c*})$$
$$\lambda_\epsilon = \gamma(1/\nu + 1, 1/\nu q_{c*}) \tag{4}$$

for $b = 2$. In these expressions, ν is streamflow variability, γ is an exponent that describes how the at-a-station channel width varies with the daily variations in streamflow and q_{c*} is the critical (or threshold) specific daily streamflow for erosion normalized by mean daily streamflow, $q_{c*} = q_c/\mu$. $\Gamma(,)$ and $\gamma(,)$ are the upper and lower regularized incomplete gamma functions, respectively, $\Gamma_g(, ;)$ is the generalized upper regularized incomplete gamma function and $\Gamma()$ is the gamma function. $K_\nu()$ is the modified Bessel function of the second type.

Streamflow mean and variability are obtained based on a hydro-ecological model derived by Botter et al. (2007), in which daily rainfall is assumed to follow a Poisson's process of rate λ and intensity α. λ can be regarded as the mean daily rainfall frequency and α as the mean daily rainfall or storm depth. According to this model, streamflow mean, μ, and variability, ν, can be expressed as:

$$\mu = \omega \alpha_c \lambda_c$$
$$\nu = 1/(\omega \lambda_c \tau) \tag{5}$$

where ω is a dimensionless filtering factor representing the ratio of rainfall that is given back to the atmosphere through evapo-transpiration and τ is the catchment response time, which we assume to vary as a weak power of catchment size (Doulatyari et al., 2017):

$$\tau \propto A^{0.13} \tag{6}$$

λ_c and α_c are the upstream catchment integrated mean daily rainfall frequency and mean daily storm depth, that is, modified values of λ and α to take into account that the fraction of a catchment simultaneously affected by a storm decreases as catchments become bigger because storms have a characteristic size. They can be expressed as (see Appendix A):

$$\lambda_c = 1 - (1 - \lambda)^\eta$$
$$\alpha_c = \lambda \alpha / \lambda_c \tag{7}$$

where η is the ratio of upstream area, A, to storm size, A_c:

$$\eta = \max(1, A/A_c) \tag{8}$$

Following Porporato et al. (2002), the dimensionless factor ω can be expressed as:

$$\omega = \frac{\phi s_*^{s_*/\phi} e^{-s_*}}{s_* \Gamma(s_*/\phi) \gamma(s_*/\phi, s_*)} \tag{9}$$

where ϕ is the aridity index, and s_* the effective soil depth. The aridity index is the ratio of potential evapo-transpiration to mean rainfall rate ($\phi = PET/\bar{p}$, where $\bar{p} = \lambda \alpha$) and the effective soil depth is the ratio of soil depth to storm depth ($s_* = s_0/\alpha$).

3. The Critical Specific Daily Streamflow, q_{c*}

The critical streamflow, q_{c*}, can be expressed in terms of the critical shear stress, τ_c, according to:

$$q_{c*} = \left(\frac{k_e \tau_c^a}{K \mu^m A^m S^n} \right)^{1/\gamma} \tag{10}$$

This implies that, if the critical shear stress does not depend on slope, the critical discharge varies as $S^{-n\gamma}$. There is, however, some debate (Lamb et al., 2008) on the dependence of the critical shear stress on slope. This dependence is commonly expressed using the critical Shields stress, τ_{c*} (or normalized critical stress), as follows:

$$\tau_{c*} = \frac{\tau_c}{(\rho_s - \rho_w)Dg} = kS^d \tag{11}$$

where ρ_s and ρ_w are the density of sediment and water, respectively, D the mean grain size and g the gravitational acceleration. According to Miller et al. (1977), $d = 0$ and $k = 0.047$ (this corresponds to the case where the critical shear stress is independent of slope), while according to Lamb et al. (2008) two asymptotic behaviors must be considered: $d = 0.25$ and $k = 0.15$ when water height is markedly greater than grain size (typically in low slope environments) and $d = 1$ and $k = 0.7$ otherwise.

In order to maintain generality, we will assume the following expression for the normalized critical streamflow:

$$q_{c*} = \left(\frac{k_e \left(k(\rho_s - \rho_w)Dg S^d \right)^a}{K \mu^m A^m S^n} \right)^{1/\gamma} = \left(\frac{\epsilon_c}{K \mu^m A^m} \right)^{1/\gamma} S^{(ad-n)/\gamma} \tag{12}$$

where:

$$\epsilon_c = k_e(k(\rho_s - \rho_w)Dg)^a \tag{13}$$

is a quantity that has the dimension of an erosion rate. We see that if $ad - n \approx 0$, the normalized critical streamflow is independent of slope. Any other combination of d, a, and n will lead to some form of dependence of the critical streamflow, q_{c*}, on slope. In particular, and assuming that $a = 3n/2$ and $\gamma = 3/4$, several combinations that

Table 1
Dependency of the Critical Shear Stress on Slope (Exponent d in Equation 11) and Its Implication for the Dependency of Critical Stream Flow (Exponent $(ad - n)/\gamma$ in Equation 12)

Reference	d	$(ad - n)/\gamma$
Miller et al. (1977)	0	$-8n/3$
Lamb et al. (2008)	1/4	$-5n/3$
Special case	2/3	0
Lamb et al. (2008)	1	$4n/3$

are of interest to us are shown in Table 1, that is, corresponding to the hypothesis of Miller et al. (1977), or those of Lamb et al. (2008), or the special case where $d = 2/3$ which yields a critical stream flow that does not depend on slope. It shows that, across the range of accepted values for the dependence of the critical Shields stress on slope (Lamb et al., 2008), the critical specific streamflow, q_{c*}, can either decrease or increase with slope. The former seems more physically plausible than the latter. However, in high slope environments, water depth may be smaller than mean grain size leading to a decrease in the lift force caused by flowing water on bedload (Lamb et al., 2008) and, consequently, an increase in the critical specific streamflow.

Finally, it is worth noting that there might exist a power law relationship between mean grain size and slope as suggested by Scherler et al. (2017b). In this case, the critical erosion rate would take the form:

$$\epsilon_c = k_e(k(\rho_s - \rho_w)D_0 g)^a \tag{14}$$

with:

$$D = D_0 S^{d'} \tag{15}$$

and the slope dependence of q_{c*} would be expressed as:

$$q_{c*} = \left(\frac{\epsilon_c}{K \mu^m A^m} \right)^{1/\gamma} S^{(a(d+d')-n)/\gamma} \tag{16}$$

Scherler et al. (2017b) propose a value of 0.45 for d'. Here, for simplicity, we will assume that the exponent d contains both the dependence of the critical Shields stress on slope and the dependence of grain size on slope.

4. Generalized TS-SPIM

We recall that the critical daily streamflow corresponds to the minimum streamflow necessary for instantaneous erosion to take place. This implies that:

$$\epsilon = K \mu^m A^m S^n q_{c*}^\gamma - \Psi = 0 \tag{17}$$

and thus, using Equation 12,:

$$\Psi = K \mu^m A^m S^n q_{c*}^\gamma = \epsilon_c S^{ad} \tag{18}$$

Incorporating this expression for the critical streamflow into the TS-SPIM expression (Equation 1) yields:

$$<E> = K \mu^m A^m \mu_\epsilon S^n - \lambda_\epsilon \epsilon_c S^{ad} \tag{19}$$

In this way, incorporating the effect of variable discharge/rainfall into the SPIM increases its "complexity" by two additional parameters, d and ϵ_c, assuming that $a = 3n/2$.

5. The FastScape Algorithm

Braun and Willett (2013) developed an O(n)-complexity and implicit algorithm to solve the SPIM, which, can be written in its simplest form (i.e., assuming uniform precipitation and no threshold) as:

$$<E> = \partial_t h = -KA^m S^n = -KA^m \partial_x h^n \tag{20}$$

where h is the surface height and ∂_t and ∂_x are time and down-slope distance derivatives, respectively.

Using a first-order finite difference scheme between any node, i, and its so-called "downstream receiver," r, to express the slope S, they propose the simple following expression:

$$h_i(t + \Delta t) = h_i(t) - \frac{\Delta t K A_i^m}{\Delta x^n}(h_i(t + \Delta t) - h_r(t + \Delta t))^n \tag{21}$$

where Δt is the time step and Δx the distance between node i and its receiver r. The algorithm can be made O(n) in complexity by defining first a stack order s_i in which to process the nodes discretizing the landscape to (a) compute the drainage area and (b) solve the SPIM. The computation of the drainage areas is made on the landform at time t and is therefore not implicit. In the stack order any node i follows its receiver r.

In the case $n = 1$, Equation 21 reduces to:

$$h_i = h_{i,0} - F(h_i - h_r) \tag{22}$$

where h_i is the height of node i at time $t + \Delta t$, $h_{i,0}$ is the height of node i at time t, h_r is the height of the receiver of node i at $t + \Delta t$ and $F = \Delta t K A_i^m / \Delta x$, and which can be easily solved for each node i according to:

$$h_i = \frac{h_{i_0} + F h_r}{1 + F} \tag{23}$$

if nodes are processed in stack order.

In the case $n \neq 1$, Braun and Willett (2013) propose to use a Newton-Raphson iterative scheme to find the root (zero) of the function:

$$\mathcal{F} = h_i - h_{i,0} + F(h_i - h_r)^n \tag{24}$$

This leads to the following recursive formula:

$$h_i^{k+1} = h_i^k - \mathcal{F}\left(h_i^k\right) / \partial_h \mathcal{F}\left(h_i^k\right) \tag{25}$$

where $\partial_h \mathcal{F}$ is the derivative of $\mathcal{F}$ with respect to h_i obtained by differentiation:

$$\partial_h \mathcal{F}\left(h_i^k\right) = 1 + F n (h_i - h_r)^{n-1} \tag{26}$$

and $h_i^0 = h_{i,0}$.

6. Implicit Algorithm for the TS-SPIM

We propose to follow a similar approach to generalize the implicit method to the TS-SPIM. In this case and following Equation 19 the function $\mathcal{F}$ takes the form:

$$\mathcal{F} = h_i - h_{i,0} + \Delta t K \mu^m A^m \mu_\epsilon (h_i - h_r)^n / \Delta x^n - \Delta t \epsilon_c \lambda_\epsilon (h_i - h_r)^{ad} / \Delta x^{ad} \tag{27}$$

If we introduce a dimensionless variable $x = \frac{h_i - h_r}{h_{i,0} - h_r}$, this expression can be simplified to:

$$\mathcal{F} = x - 1 + F_1 \mu_\epsilon(x) x^n - F_2 \lambda_\epsilon(x) x^p \tag{28}$$

where $p = ad$ and:

$$F_1 = \frac{\Delta t K \mu_i^m A_i^m}{h_{i,0} - h_r} S_0^n$$
$$F_2 = \frac{\Delta t \epsilon_c}{h_{i,0} - h_r} S_0^p \tag{29}$$

where $S_0 = \frac{h_{i,0} - h_r}{\Delta x}$. The critical streamflow can be expressed as:

$$q_{c*} = \left(\frac{F_2}{F_1}\right)^{1/\gamma} x^{(p-n)/\gamma} \tag{30}$$

The iterative Newton-Raphson scheme takes the following form:

$$x_{k+1} = x_k - \frac{\mathcal{F}(x_k)}{\partial_x \mathcal{F}(x_k)} \tag{31}$$

with $x_0 = 1$ and:

$$\partial_x \bar{\mathcal{F}} = 1 + F_1 \left(\mu_\epsilon n x^{n-1} + \partial_x \mu_\epsilon x^n \right) - F_2 \left(\lambda_\epsilon p x^{p-1} + \partial_x \lambda_\epsilon x^p \right) \tag{32}$$

with the factors μ_ϵ and λ_ϵ given in Equations 2–4 for the different values of b and:

$$\partial_x \mu_\epsilon = \partial_{q_{c*}} \mu_\epsilon \partial_x q_{c*} \text{ and } \partial_x \lambda_\epsilon = \partial_{q_{c*}} \lambda_\epsilon \partial_x q_{c*} \tag{33}$$

where:

$$\partial_{q_{c*}} \mu_\epsilon = -\frac{e^{-q_{c*}/v}(q_{c*}/v)^{1/v+\gamma-1}}{\Gamma(1/v)v^{-\gamma}} \quad \text{if } b = 1$$

$$\partial_{q_{c*}} \mu_\epsilon = -\frac{q_{c*}^{\gamma-1}e^{-2\sqrt{q_{c*}}(1+1/q_{c*})/v}}{2vK_{-1}(4/v)} \quad \text{if } b = 1.5 \tag{34}$$

$$\partial_{q_{c*}} \mu_\epsilon = -\frac{e^{-1/vq_{c*}}(1/vq_{c*})^{1/v-\gamma+2}}{\Gamma(1/v)v^{\gamma-2}} \quad \text{if } b = 2$$

and:

$$\partial_{q_{c*}} \lambda_\epsilon = -\frac{e^{-q_{c*}/v}(q_{c*}/v)^{1/v-1}}{\Gamma(1/v)} \quad \text{if } b = 1$$

$$\partial_{q_{c*}} \lambda_\epsilon = -\frac{e^{-2\sqrt{q_{c*}}(1+1/q_{c*})/v}}{2q_{c*}vK_{-1}(4/v)} \quad \text{if } b = 1.5 \tag{35}$$

$$\partial_{q_{c*}} \lambda_\epsilon = -\frac{ve^{-1/vq_{c*}}(1/vq_{c*})^{1/v+2}}{\Gamma(1/v+1)} \quad \text{if } b = 2$$

and:

$$\partial_x q_{c*} = q_{c*} \left(\frac{p-n}{\gamma} \right) x^{-1} \tag{36}$$

When convergence is reached, that is, when:

$$\epsilon_k = |x_{k+1} - x_k| < tol \tag{37}$$

where tol is a specified tolerance, the new height can be obtained from:

$$h_i = x_{k+1}(h_{i,0} - h_r) + h_r \tag{38}$$

A flow chart is given in Appendix B describing the successive steps of the algorithm for ready implementation. We also provide a *Python* implementation in a Jupyter Notebook (Braun, 2023).

Note that when $p(=ad) = n$, the critical streamflow, q_{c*} does not depend on slope and therefore not on x. In this case, Equation 27 becomes:

$$\mathcal{F} = h_i - h_{i,0} + F'(h_i - h_r)^n \tag{39}$$

with

$$F' = \Delta t (K \mu^m A^m \mu_\epsilon - \epsilon_c \lambda_\epsilon)/\Delta x^n \tag{40}$$

independent of h_i. This, in turn, implies that we can write:

$$\partial_h \mathcal{F} = 1 + F'n(h_i - h_r)^{n-1} \tag{41}$$

and apply the Newton-Raphson algorithm used in the SPIM case (Equation 25) while simply replacing F by F'.

At this point, we must acknowledge that there exists no efficient algorithm to compute the value of the generalized upper regularized incomplete gamma function, $\Gamma_g(,;)$. For the commonly accepted value of $\gamma = 0.75$, which leads to $2\gamma - 1 = 0.5$, a finite expansion can be used to compute $\Gamma_g(0.5,;)$ but cannot be used to compute $\Gamma_g(-1,;)$

as required for the computation of λ_ϵ when $b = 1.5$. In the case, $b = 1.5$, approximate expressions can be derived for μ_ϵ and λ_ϵ that are only valid for large values of the normalized specific daily streamflow, $q_{c*} \gg 1$ (Lague et al., 2005). This leads to:

$$\mu_\epsilon = \frac{\Gamma(a + \gamma')}{\Gamma(a)v' - \gamma'}\Gamma\left(a + \gamma', q_{c*}^{2-b}/v'\right)$$
$$\lambda_\epsilon = \Gamma\left(a, q_{c*}^{2-b}/v'\right)$$

(42)

where $v' = v/(2 - b)$, $\gamma' = \gamma/(2 - b)$ and $a = (1 - b)/(2 - b)$. In the rest of the manuscript we will therefore only consider the cases $b = 1$ and $b = 2$.

7. Convergence Rate of the Newton-Raphson Scheme

7.1. Original FastScape Algorithm

In the original FastScape algorithm, the function for which a root must be found (Equation 24) can be expressed in its dimensionless form:

$$\mathcal{F} = x - 1 + \hat{F}x^n$$

(43)

with:

$$\hat{F} = \frac{\Delta t K A^m}{h_{i,0} - h_r}S_0^n$$

(44)

The optimum convergence of the Newton-Raphson scheme is known to be quadratic such that the errors at successive iterations follow the following relationship (see Appendix C for derivation):

$$|\epsilon_{k+1}| \leq L\epsilon_k^2$$

(45)

where:

$$L = \sup_{x \in [0,1]} \frac{1}{2}\left|\frac{\partial_x^2 \hat{\mathcal{F}}}{\partial_x \hat{\mathcal{F}}}\right|$$

(46)

Equation 45 implies, however, that convergence is conditional to:

$$L|\epsilon_0| < 1$$

(47)

In the case of the FastScape algorithm:

$$L = \sup_{x \in [0,1]} \frac{1}{2}\left|\frac{n(n-1)\hat{F}x^{n-2}}{1 + n\hat{F}x^{n-1}}\right| = \frac{1}{2}\frac{n(n-1)\hat{F}}{1 + n\hat{F}}$$

(48)

and, because $x_0 = 1$:

$$|\epsilon_0| = \left|\frac{\hat{\mathcal{F}}(1)}{\partial_x \hat{\mathcal{F}}(1)}\right| = \frac{\hat{F}}{1 + n\hat{F}}$$

(49)

This leads to the following condition for convergence:

$$L|\epsilon_0| = \frac{1}{2}\frac{n(n-1)\hat{F}^2}{\left(1 + n\hat{F}\right)^2} < 1$$

(50)

which is satisfied for all values of $\hat{F} \in [0, +\infty[$, as:

$$\lim_{\hat{F}\to 0} L|\epsilon_0| = 0 \quad \text{and} \quad \lim_{\hat{F}\to\infty} L|\epsilon_0| = \frac{1}{2}\frac{(n-1)}{n} < 1, \quad \text{for all } n \geq 1$$

(51)

Note also that Equation 45 implies that the rate of convergence is proportional to L^{-1}.
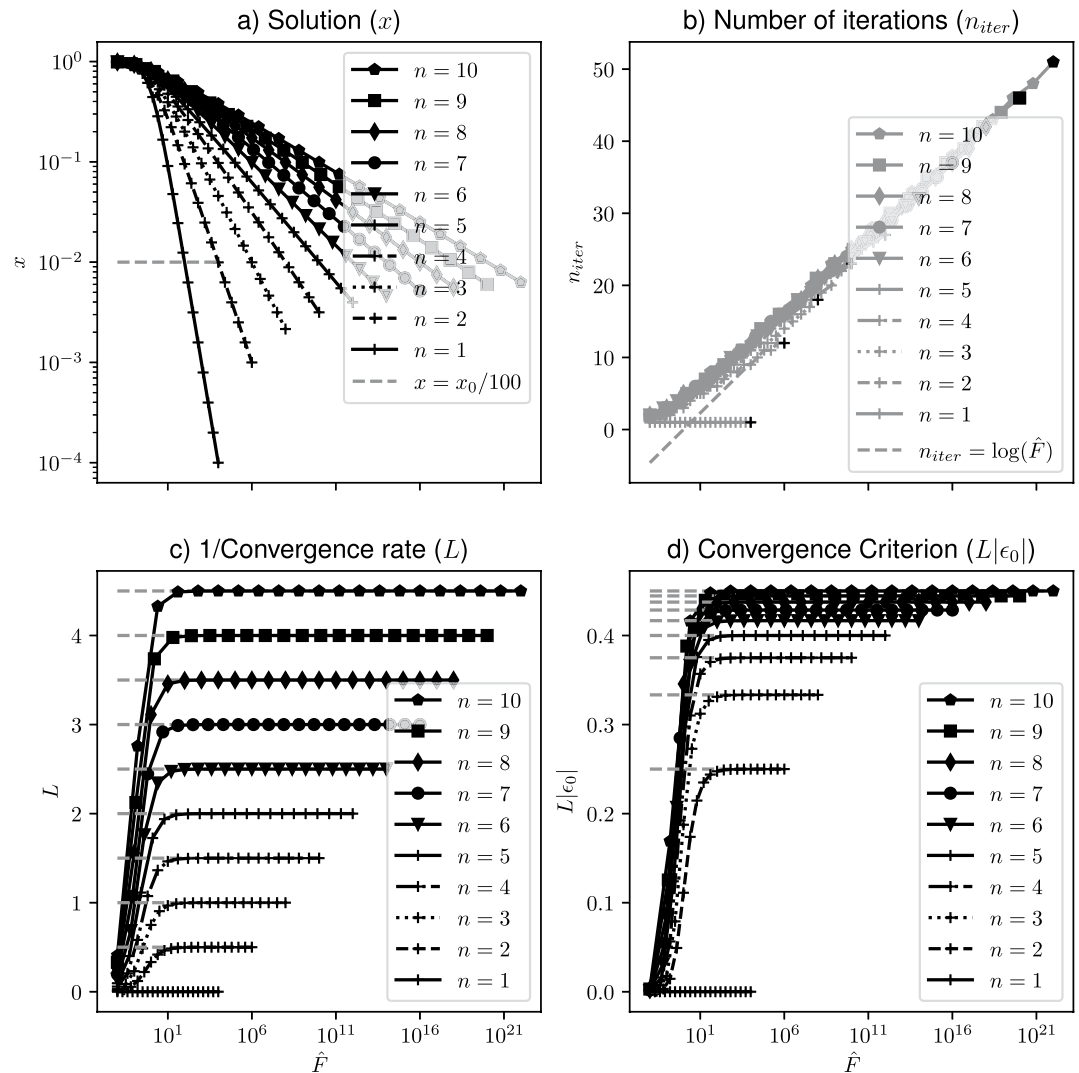
Figure 1. (a) Solution of the non-linear stream power incision model after one time step as a function of $\hat{F}$ (Equation 44) and various values of n. (b) Corresponding number of iterations required to achieve convergence ($\epsilon_{n_{iter}} < 10^{-6}$; the black symbols correspond to the value obtained for the largest value of $\hat{F}$ over the range considered. (c) Inverse of the convergence rate computed according to Equation 46; the gray dashed lines correspond to the asymptotic value s for $\hat{F} \rightarrow \infty$ (d) Initial converge criterion, $L|\epsilon_0|$ computed according to Equation 50; the gray dashed lines correspond to the asymptotic values for $\hat{F} \rightarrow \infty$.

In Figure 1a, we show the solution of the non-linear SPIM over one time step as a function of $\hat{F}$ for different values of the exponent n. For each n value, the range of values for $\hat{F}$ has been adjusted such that the solution decreases at least by two orders of magnitude over the range of $\hat{F}$ values. The number of iterations required to reach convergence, n_{iter} is shown in Figure 1b assuming that convergence is reached when $\epsilon_{n_{iter}} < 10^{-6}$. The number of iterations grows asymptotically as $\log\left(\tilde{F}\right)$ (gray dashed line) and grows linearly with n. In Figures 1c and 1d, we show L and $L|\epsilon_0|$ for the same range of $\hat{F}$ and n values. The gray dashed lines in Figures 1c and 1d are the asymptotic values for L and $L|\epsilon_0|$, respectively, when $F \rightarrow \infty$. Most importantly, we see that (a) the convergence criterion is, indeed, always fulfilled, that is, for all $n > 1$ and regardless of the value of $\tilde{F}$ (Figure 1d) and (b) the asymptotic rate of convergence (i.e., for $\tilde{F} \rightarrow \infty$) decreases linearly as $1/n$ (Figure 1c). Note that, although we do not show it in Figure 1a, we checked that this remains true for non-integer values of $n > 1$.

7.2. Generalized TS-SPIM FastScape Algorithm But First Neglecting the Slope Dependence in μ_ϵ and λ_ϵ

If we neglect the dependence on slope of μ_ϵ and λ_ϵ (through their dependence on q_{c*}) in the generalized TS-SPIM FastScape algorithm, the function for which a root must be found (Equation 24) has the form:

$$\mathcal{F} = x - 1 + \hat{F}_1 x^n - \hat{F}_2 x^p \tag{52}$$

where:

$$\hat{F}_1 = \frac{\Delta t K \mu^m A^m \mu_\epsilon}{h_{i,0} - h_r} S_0^n \tag{53}$$

and:

$$\hat{F}_2 = \frac{\Delta t \epsilon_c \lambda_\epsilon}{h_{i,0} - h_r} S_0^p \tag{54}$$

Note that, with this notation, the condition $\hat{F}_1 > \hat{F}_2$ must be fulfilled for erosion to take place.

We now write the corresponding expressions for L and $|\epsilon_0|$:

$$L = \frac{1}{2} \left| \frac{n(n-1)\hat{F}_1 - p(p-1)\hat{F}_2}{1 + n\hat{F}_1 - p\hat{F}_2} \right| \tag{55}$$

and

$$|\epsilon_0| = \left| \frac{\hat{F}_1 - \hat{F}_2}{1 + n\hat{F}_1 - p\hat{F}_2} \right| \tag{56}$$

The condition for convergence becomes:

$$L|\epsilon_0| = \frac{1}{2} \frac{\left(\hat{F}_1 - \hat{F}_2\right)|n(n-1)\hat{F}_1 - p(p-1)\hat{F}_2|}{\left(1 + n\hat{F}_1 - p\hat{F}_2\right)^2} < 1 \tag{57}$$

Introducing the ratios $r = p/n$ and $\hat{\zeta} = \hat{F}_2/\hat{F}_1$, this condition can be simplified by considering only its asymptotic value, that is,:

$$\lim_{\hat{F}_1, \hat{F}_2 \to \infty} L|\epsilon_0| = \frac{1}{2} \frac{(1-r)|1 - 1/n - \zeta\left(\hat{\zeta} - 1/n\right)r|}{\left(1 - \hat{\zeta}r\right)^2} \tag{58}$$

In Figure 2, we map this condition in the $[r, \hat{\zeta}]$-space for two extreme values of n, that is, $n = 1$ and 10. We consider values of $r \in [-1, 2]$ and $\hat{\zeta} \in [0, 1]$. We see that the condition is always fulfilled and the Newton-Raphson scheme is unconditionally convergent when the ratio $r = p/n < 1$. For values of $p > n$ (or $r > 1$), the scheme does not converge (i.e., $L|\epsilon_0| > 1$) in the range corresponding to the gray hatched area in Figure 2. We see that this region does not depend much on n.

Considering the plausible values of $p = ad$ given in Table 1, we see that our proposed scheme is suitable and unconditionally convergent except for the special case when $p = ad = 3n/2 > n$ that is suggested by Lamb et al. (2008)'s work in high slope, low flow thickness environments.

7.3. Generalized TS-SPIM Algorithm

In this case, the function for which a root must be found has the form:

$$\mathcal{F} = x - 1 + F_1 \mu_\epsilon(x) x^n - F_2 \lambda_e(x) x^p \tag{59}$$

and to estimate the convergence criterion, we need to compute $\partial_x^2 \mathcal{F}$. The procedure is shown in Appendix D.

In Figures 3 and 4, we show where the convergence criterion is not met (the dark gray hatched region), that is, where $L|\epsilon_0| > 1$, in the space $[r, \zeta]$, where $r = p/n$ and $\zeta = F_2/F_1$, for various values of n, ν, and b, and assuming
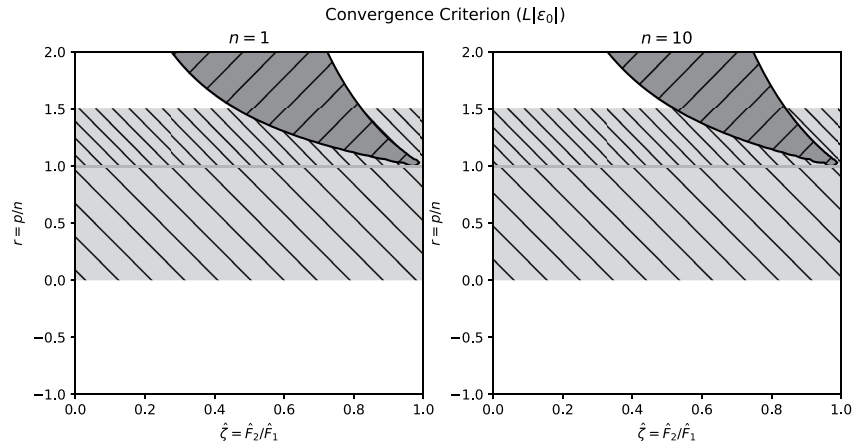
Figure 2. Regions of the $\left[\hat{\zeta}, r\right]$ space where the condition for stability of the Newton-Raphson's root finding scheme is not met (dark gray hatch area) and region of physically meaningful values of the $\hat{\zeta}$ and r parameters (light gray shaded area) for a $n = 1$) and (b) $n = 10$. The densely shaded area corresponds to the case envisaged by Lamb et al. (2008) leading to a critical streamflow increasing with slope (i.e., high slope, low flow depth). We note that the region of overlap corresponding to situations that are physically plausible but where the iterative scheme diverges are limited to that part of the parameter space.

$\gamma = 1$. We see that including the full dependence of μ_ϵ and λ_ϵ on S does not restrict the conditions for convergence of the Newton-Raphson algorithm. In fact the region of parameter space where convergence is not guaranteed shrinks as streamflow variability, ν, increases for both values of the b exponent considered here, that is, 1 and 2.

8. Algorithm Accuracy

8.1. Original FastScape Algorithm

The efficiency of the implicit FastScape algorithm (Braun & Willett, 2013) comes at the cost of its accuracy, as demonstrated by Campforts and Govers (2015). The FastScape algorithm uses a first order accurate estimate of the slope and in the direction opposite to the transfer of information by upstream advection. As shown by Campforts and Govers (2015) and in Figure 5a, the algorithm produces an unwanted numerical smoothing or diffusion of knickpoints. In Figure 5a, we compare the solution obtained with the FastScape algorithm to an analytical solution (from Royden and Perron (2013)) for the propagation of a knickpoint following the instantaneous and uniform uplift of an initially flat area of which one point is kept at a constant, nil elevation (the base level). The FastScape solution is also compared to the solution obtained with the TVD (Total Variation Diminishing) algorithm proposed by Campforts and Govers (2015). The TVD algorithm performs much better than the FastScape algorithm in the vicinity of the knickpoint. This difference is, however, much smaller for larger values of the SPIM slope exponent, n. In Figure 5b, we show the same comparison for $n = 2$.

The error is also a function of the time step length and the grid spacing. In Figure 6, we show contour plots of the error, ϵ_F, computed from:

$$\epsilon_F = <\max_{x \in L}\frac{|h - h_a|}{\max h_a}>$$

(60)

where $<>$ is the mean value over all time steps.

We see that error is between half to an order of magnitude smaller for the TVD algorithm compared to the FastScape algorithm, as already demonstrated by Campforts and Govers (2015). As the slope exponent is increased, the difference is much reduced as the error obtained with the FastScape algorithm is less than 1% for all reasonable values of time and space discretization ($nstep > 30$ and $nx > 30$).

Being explicit in time, the TVD method can only be used if the time step satisfies the *CFL* condition, which is in this case:

$$CFL = \frac{\Delta t}{\Delta x}\max_{x \in L}\left(KA^m S^{n-1}\right) < 1$$

(61)

Convergence Criterion ($L|\epsilon_0|$) for b=1
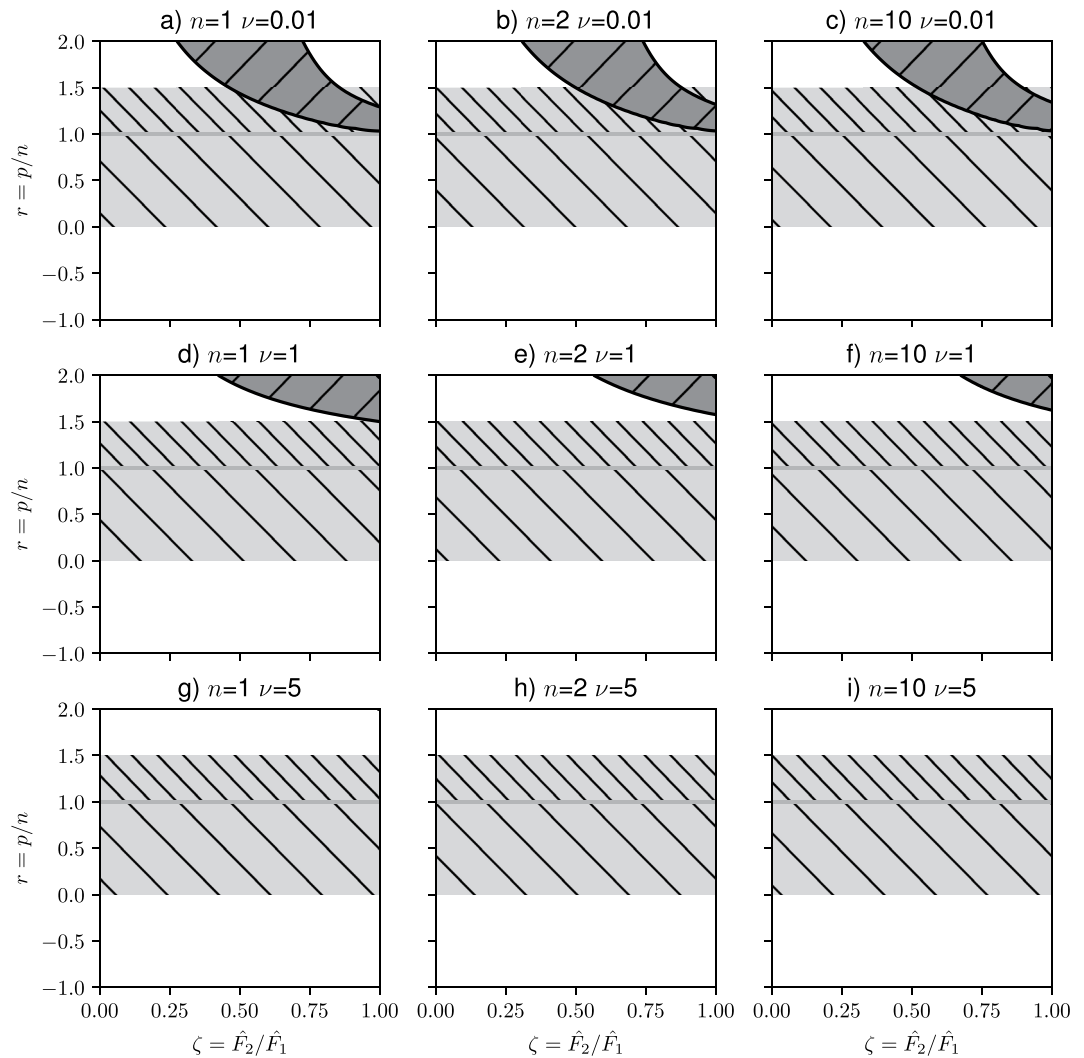
Figure 3. Regions of the $[\hat{\zeta}, r]$ space where the condition for stability of the Newton-Raphson's root finding scheme is not met (dark gray hatch area) and region of physically meaningful values of the $\hat{\zeta}$ and r parameters (light gray shaded area). The densely shaded area corresponds to the case envisaged by Lamb et al. (2008) leading to a critical streamflow increasing with slope (i.e., high slope, low flow depth). Each panel, (a) to (i), correspond to specific and representative values of n and ν, the streamflow variability, as indicated. In this figure $b = 1$ is assumed.
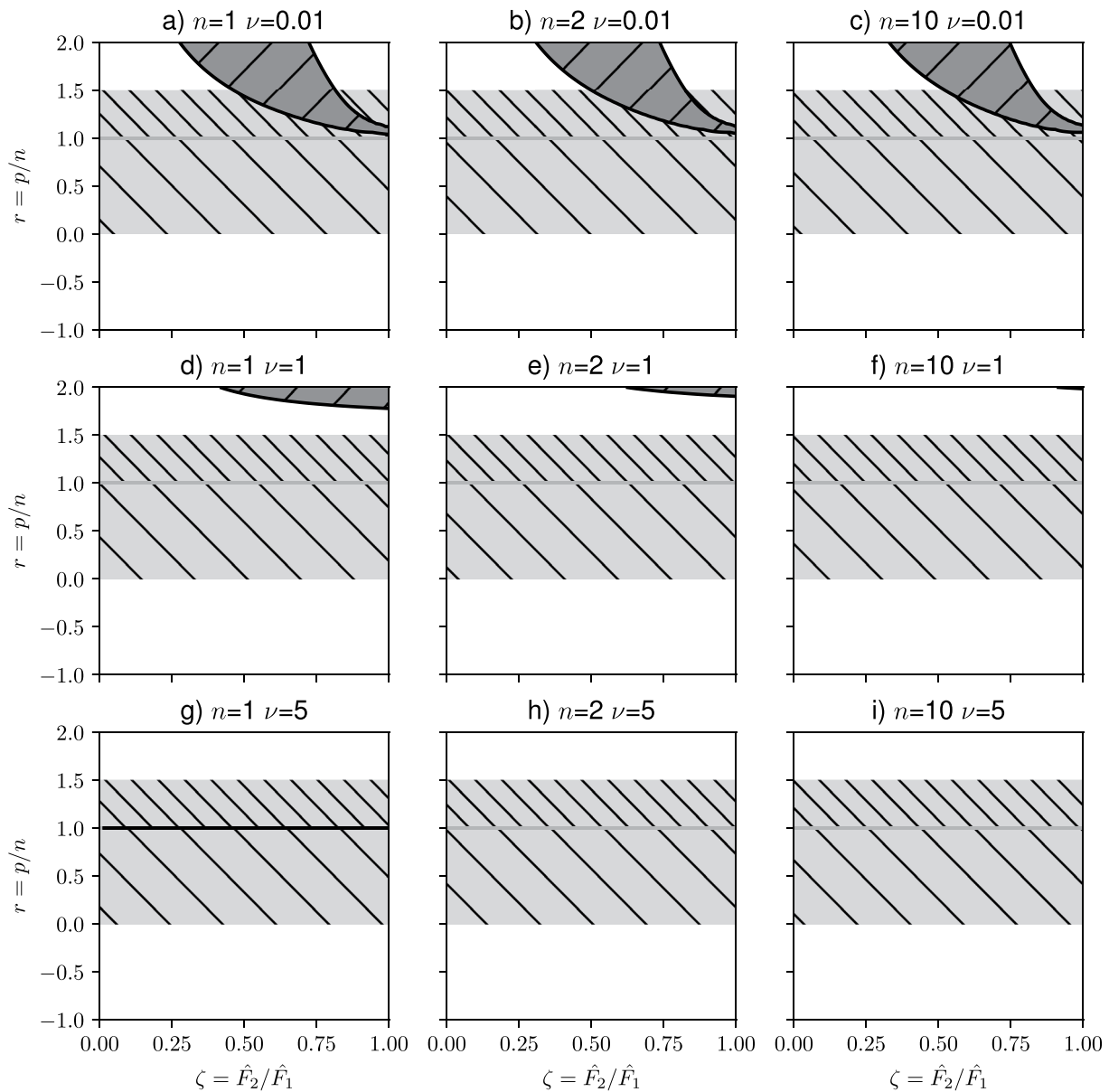
as shown by Campforts and Govers (2015). The *CFL* condition corresponds to combinations of *nstep* and *nx* above the black line diagonally crossing each panel in Figure 6. Being implicit in time, the FastScape algorithm is unconditionally stable and its accuracy increases with a diminishing time step but is independent of spatial resolution when *CFL* < 1 and increases with diminishing grid spacing but is independent of time step length when *CFL* > 1.

8.2. Generalized SPIM

There is no simple analytical solution to the generalized SPIM, that is, Equation 19. We can, however, assess the accuracy of the implicit algorithm using an analytical solution to the following equation:

$$\frac{\partial h}{\partial t} = U - KA^m S^n + VS \tag{62}$$

Figure 4. Regions of the $[\hat{\zeta}, r]$ space where the condition for stability of the Newton-Raphson's root finding scheme is not met (dark gray hatch area) and region of physically meaningful values of the $\hat{\zeta}$ and r parameters (light gray shaded area). The densely shaded area corresponds to the case envisaged by Lamb et al. (2008) leading to a critical streamflow increasing with slope (i.e., high slope, low flow depth). Each panel, (a) to (i), correspond to specific and representative values of n and ν, the streamflow variability, as indicated. In this figure $b = 2$ is assumed.

that has the same form as Equation 19 in the sense that it is the sum of two terms, one dependent on slope to power n and drainage area to power m and one dependent on slope to power 1. In fact this equation represents a variant of the SPIM in which a term representing the horizontal advection of the surface (at a rate V) has been added. For example, in a simple situation where uplift is due to movement of a thrust fault dipping at angle ψ, U, and V are related by a simple relationship:

$$V \sin \psi = U \cos \psi \tag{63}$$
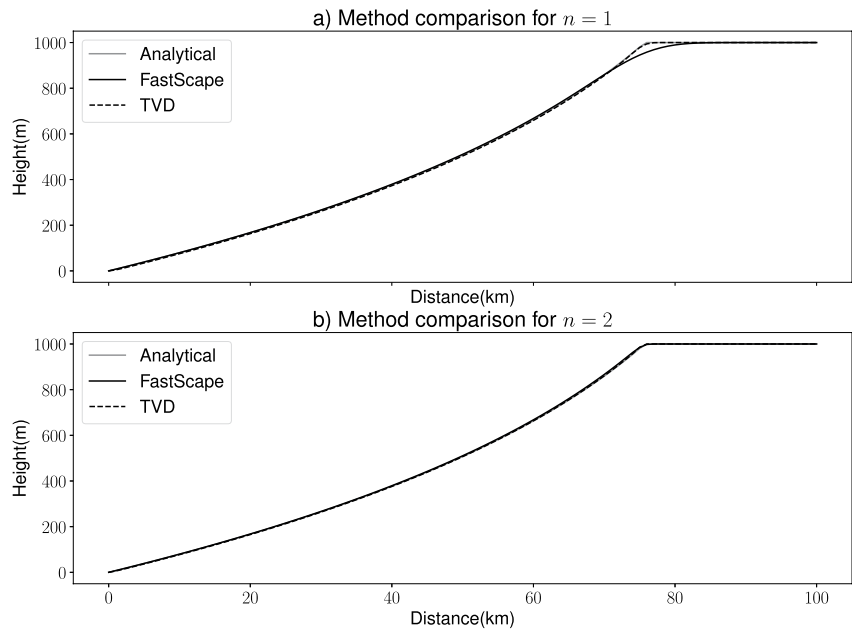
Figure 5. Comparison between an analytical solution, the FastScape algorithm and the TVD method proposed by Campforts and Govers (2015) to a simple knickpoint propagation problem from an initially flat topography subject to an instantaneous, uniform uplift at time $t = 0$. Time and space resolutions of 2000 time steps and 100 grid points to cover a 1 Myr total run time and a $L = 100$ km spatial domain, are used. In panel (a) the stream power incision model slope exponent, n, is 1; in panel (b) the slope exponent is 2. The area exponent, m, has been scaled such that the concavity is 0.45 in both cases, and the rate coefficient, K has also been scaled such that the knickpoint propagates to an identical distance.

Making use of Hack's law, that is, $A = k(L - x)^p$, we can write this equation under the following form:

$$\frac{\partial h}{\partial t} = U - Kk^m(L - x)^{mp}S^n + VS \tag{64}$$
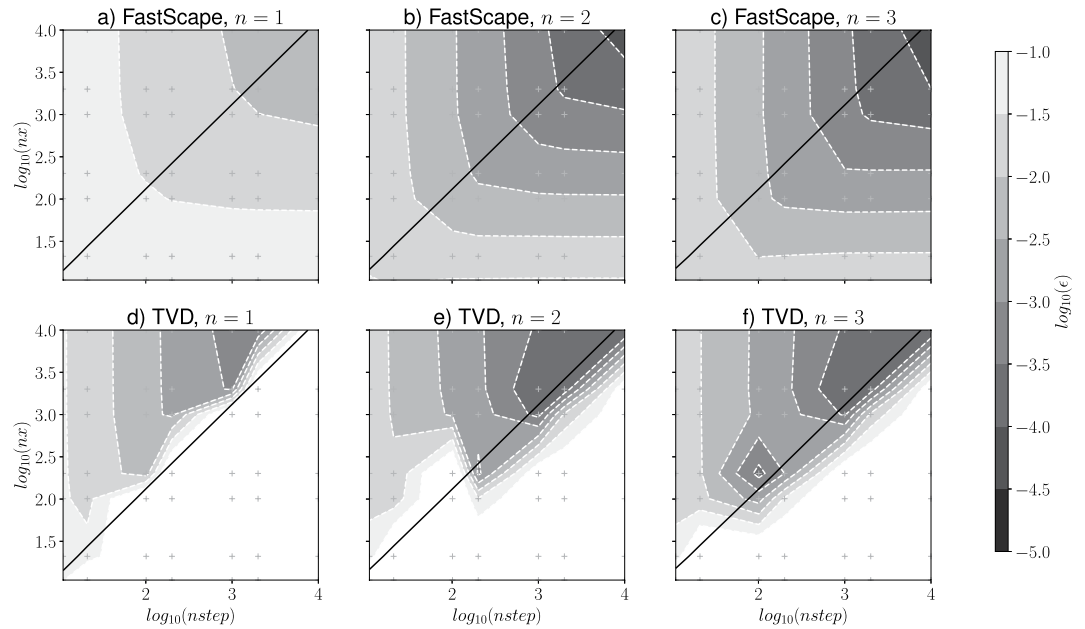
Figure 6. Contour plots of the error estimated computed from Equation 60 using the FastScape algorithm (a to c) and the TVD algorithm (d to f). In each panel, the region above and below the black line correspond to $CFL < 1$ and $CFL > 1$, respectively. The small crosses give the position of the 49 discrete values of $nstep$ and nx used to compute the contour plots.
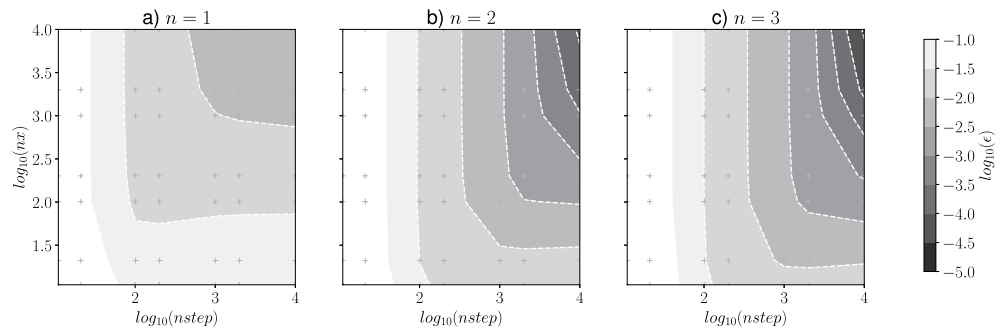
Figure 7. Contour plots of the error estimated computed from Equation 60 using the generalized FastScape algorithm for different values of n(a to c). The small crosses give the position of the 49 discrete values of *nstep* and *nx* used to compute the contour plots.

which has a steady-state analytical solution for $n = 1$, 2 or 3 under the assumption of uniform uplift at a rate U and horizontal advection at a velocity V. The transient solution is made of two parts: the region below the knickpoint has reached steady-state while the region above the knickpoint is at a uniform elevation given by Ut.

In Figure 7, we show the error resulting from the implicit solution. We see that the error decreases with increasing temporal resolution (i.e., decreasing time step length) but is rather insensitive to the spatial resolution, except when $n = 1$. As in the original FastScape algorithm, the error decreases drastically with increasing n.

9. Example of Use of the New Algorithm: Effect of an Erosional Threshold on the Decay Rate of Orogenic Systems

The topographic longevity of many ancient orogenic systems, such as the Dabie Shan (Braun & Robert, 2005) or the Pyrenees (Curry et al., 2019), remains enigmatic. Although erosion-driven, post-orogenic isostatic rebound affects the rate of topographic decay (Ahnert, 1970), it is widely accepted that it is the efficiency of erosional processes that exerts the primary control (Wolf et al., 2022). Some have argued that the efficient of hillslope processes such as landsliding and the characteristics of the material they provide to the channels play an important role in protecting bedrock from erosion (the so-called "cover effect") or enhancing it (the "tool effect") and therefore play a critical role in maintaining topographic relief once uplift has ceased (Egholm et al., 2013). As shown by Baldwin et al. (2003), the existence of an erosional threshold, represented in their study by the inclusion of a critical shear stress in the stream power law, may cause a channel to maintain significant relief over periods that far exceed the characteristic time for mountain growth (of the order of a few millions of years). Here, using our newly developed algorithm, we present the results of a series of two-dimensional numerical experiments in order to confirm and generalize this result to the mountain scale.

In Figures 8a and 8b, we first show how the SPIM slope exponent, n, influences the longevity of the post-orogenic phase of a mountain belt. For this, we performed simple 2D experiments using the FastScape algorithm in which a small orogenic area of size 10×10 km (discretized by 101×101 points) is subjected to uplift at a rate of 10^{-3} m/yr for a period of 20 Myr (discretized by 101 time steps) at which point the uplift rate is set to zero. The SPIM slope exponent, n, varies between experiments from 1 to 5. The area exponent, m varies also to keep the ratio m/n constant at 0.45, while the rate constant K varies between 10^{-5} and 10^{-13} m^{2-m}/yr in order to create a mountain belt that has approximately the same mean steady-state topography in all experiments. In Figure 8a, we show the temporal evolution of the mean topography for five of these experiments corresponding to integer values of n between 1 and 5. We see that during the growth phase the mean topography increases as an exponential function of time:

$$h_{mean} \propto 1 - e^{-t/\tau} \tag{65}$$

where τ is of the order of 2–3 Myrs, regardless of the value of n. On the contrary, the evolution of the decay phase varies strongly with n and leads to a finite residual topography at time $t = 50$ Myr or at a time equal to $10 \times \tau$ after the end of the orogenic phase that increases with n. One can show (see Appendix E) that the rate of topographic decay follows a power law of the form:

$$h_{mean} \propto (1 + (n - 1)\pi t/\tau)^{1/(1-n)} \tag{66}$$
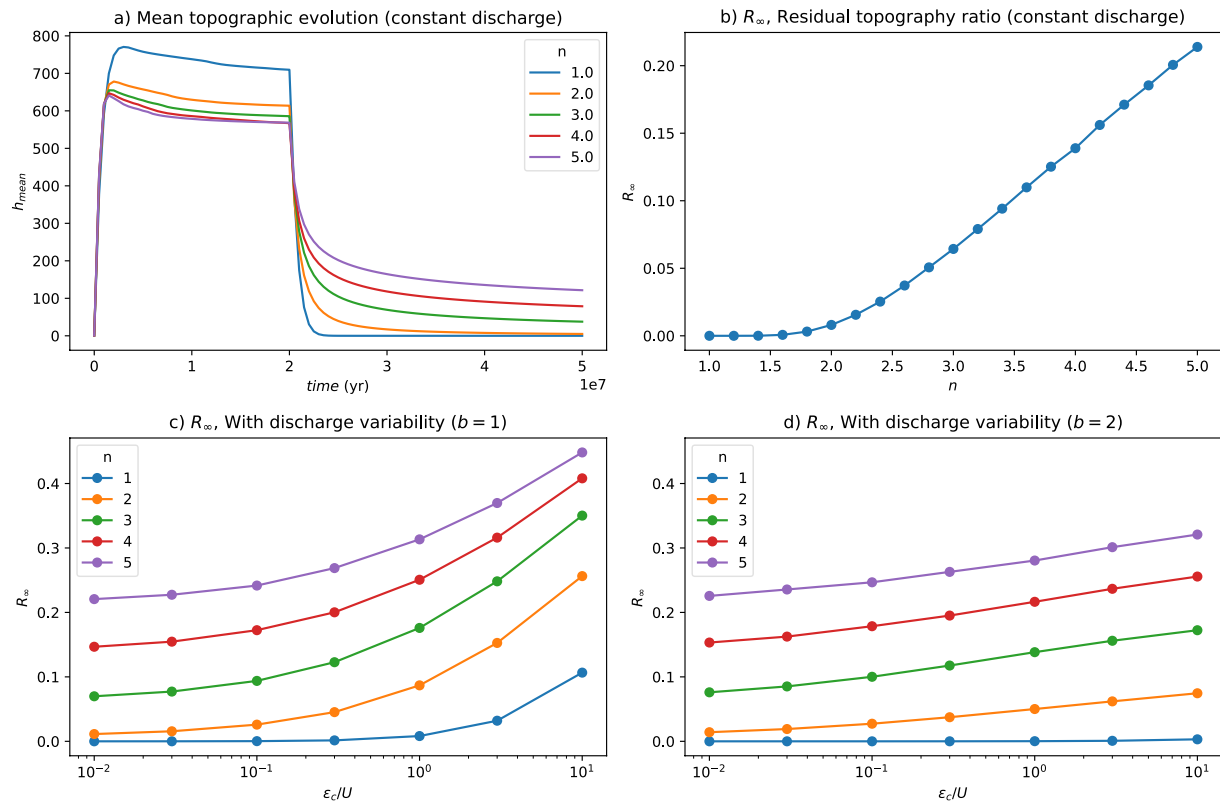
Figure 8. (a) Time evolution of mean topography in a 2D orogen during orogenic growth and decay, for various values of the stream power incision model slope exponent, n. (b) Ratio, R_∞, of mean topography at the end of the experiment and at the end of orogenic phase as a function of n. (c) Computed values of R_∞, the ratio of preserved to steady-state mean topography as a function of ϵ_c normalized by the imposed uplift rate, U for the case $b = 1$ and (d) for the case $b = 2$.

rather than an exponential law. In Figure 8b, we show the ratio of this residual mean topography to the steady-state orogenic mean topography for 20 values of n between 1 and 5 to demonstrate the quasi linear relationship between R_∞ and n. Although interesting, this result cannot easily explain the longevity of post-orogenic topography as commonly accepted values of n are in the range [1–2], which implies that only a few percent of the steady-state topography could be preserved by invoking this mechanism.

We performed another set of experiments in which we introduced an erosional threshold to quantify how the value of the threshold may influence the amplitude of the residual topography. For this, we performed another set of experiments varying n (and thus m and K) but also the value of ϵ_c (Equation 13) while keeping the parameters controlling stream flow variability and its effect on erosion constant, that is, $\lambda = 0.2$ per day, $\alpha = 10$ mm, $PET = 1$ mm/day, $s_0 = 10$ mm, $ad = 3n/8$ and $\gamma = 0.75$. We assumed a storm size much bigger than the mountain area so that the effect of a finite storm size is neglected and we present results for two values of the recession exponent, that is, $b = 1$ and 2.

Results are shown in Figures 8c and 8d as plots of the preserved topographic ratio, R_∞, against the threshold erosion rate, ϵ_c normalized by the uplift rate, for the two values of the recession exponent, b. We see that as the assumed threshold increases, the proportion of the steady-state topography that is preserved 30 Myr after the end of the orogenic phase also increases. This increase is much greater and shows a greater rate of increase as a function of ϵ_c for $b = 1$ than for $b = 2$.

Most interestingly, in the case where $n = 2$, which is likely to be most representative of the natural system, R_∞ can be as high as 0.25 (i.e., a quarter of the steady-state topography is preserved 30 Myr after the end of the orogenic phase) when the critical erosion rate, ϵ_c is 10 times the value of the uplift rate. This implies that, even for a reasonable/small value of n, the presence of a finite erosional threshold can lead to preservation of a substantial amount of post-orogenic topography for tens or even hundreds of millions of years, confirming the results obtained by Baldwin et al. (2003).

10. Discussion and Conclusions

We have shown that the FastScape algorithm can be generalized to take into account the existence of an erosional discharge threshold under variable discharge conditions, even if the threshold is a function of channel slope. The algorithm remains O(n) in complexity and is implicit in time. To achieve this, we need to find the root of a highly non-linear function by a Newton-Raphson iterative algorithm. We have shown that, for the original FastScape algorithm, the convergence is unconditional and its rate varies linearly with the value of n, the slope exponent in the SPIM. For the generalized TS-SPIM, the convergence of the Newton-Raphson algorithm is also unconditional except when the threshold is a positive function of channel slope (as suggested by Lamb et al. (2008)) and when discharge variability is low.

We have also confirmed the findings of Campforts and Govers (2015) concerning the relative low accuracy of the FastScape algorithm but demonstrated that it becomes similar to that of other higher-order algorithms for values of the slope exponent, n, larger than 1. It is also important to remind the reader that, due to its implicit nature, the FastScape algorithm provide a stable and accurate solution to the SPIM and TS-SPIM for time steps/spatial discretization that do not satisfy the *CFL* condition, contrary to other higher-order algorithms.

This work demonstrates that even complex non-linear erosion laws can be rendered implicit and O(n) complexity based on a generalized version of the FastScape algorithm. Hergarten (2020) has shown that even transport-limited and under-capacity laws can also be rendered implicit and O(n) complexity but in the spacial case of a linear dependence on channel slope only. Future work should be devoted to generalize this finding to any slope exponent n in the SPIM formulation and to the more useful case of multiple direction flow when dealing with sediment transport and deposition. Using the approach presented here could provide an effective solution.

Appendix A: Averaging Uncorrelated and Correlated Rainfall

The probability of rainfall occurring at point i is λ_0, and the probability of rainfall depth when rainfall occurs is:

$$f_{X_0}(X_0 = x_0) = \frac{1}{\alpha_i} e^{-x_0/\alpha_0} \tag{A1}$$

Thus the probability of rainfall at point i is a random variable described by the following probability distribution:

$$f_{x_0}(X_0 = x_0) = \frac{\lambda_0}{\alpha_i} e^{-x_0/\alpha_0} + (1 - \lambda_0)\delta(0) \tag{A2}$$

where the second term represents the atom of probability that there is no rainfall. Here we want to track the depth of rainfall relative to the catchment we want to upscale to, so we introduce a new variable $x = A_0 x_0/A$ where A is the area of the large catchment, and A_0 is the small area associated with the point rainfall statistics. Using this new variable, we can write:

$$f_X(X = x) = \frac{A\lambda_0}{A_0\alpha_0} e^{-Ax/\alpha_0 A_0} + (1 - \lambda_0)\delta(0) \tag{A3}$$

we now make the assumption that rainfall is perfectly correlated up to some scale, A_c, above which it is independent. Thus, as long as $A \leq A_c$, we can write:

$$f_X(X = x) = \frac{\lambda_0}{\alpha_0} e^{-x/\alpha_0} \tag{A4}$$

When $A > A_c$, rainfall is made of uncorrelated storms of size A_c, which can be regarded as an "average storm size" and is the convolution of n distributions. Considering first two such rainfall events, we can write:

$$f_Z(z) = f_X * f_X = (\lambda f_{X,1} + (1 - \lambda)f_{X,0}) * (\lambda f_{X,1} + (1 - \lambda)f_{X,0}) \tag{A5}$$

where $n = A/A_c$, $f_{X,1} = \frac{n}{\alpha_0} e^{-nx/\alpha_0}$ and $f_{X,0} = \delta(0)$. This leads to:

$$f_Z(z) = \lambda^2(f_{X,1} * f_{X,1}) + 2\lambda(1 - \lambda)(f_{X,1} * f_{X,0}) + (1 - \lambda^2)(f_{X,0} * f_{X,0}) \tag{A6}$$

As $f_{X,0} = \delta(0)$, we can write that $f_{X,0} * f_{X,0} = \delta(0)$ and $f_{X,1} * f_{X,0} = fX, 1$, while $f_{X,1} = \left(\frac{n\lambda_0}{\alpha_0}\right)^2 \frac{x}{\Gamma(2)} e^{-nx/\alpha_0}$ as the convolution of two exponential functions is the gamma function.

We can now generalize this result for n rainfall events, which gives:

$$f_Z(z) = (f_X)^n = \left(1 - (1 - \lambda_0)^n\right) \frac{a_n(x)}{c_n} e^{-nx/\alpha_0} \tag{A7}$$

where:

$$a_n(x) = \sum_{k=0}^{n} \frac{\binom{n}{k}}{\Gamma(k)} \left(\frac{\lambda_0}{1 - \lambda_0}\right)^k \left(\frac{nx}{\alpha_0}\right)^{k-1} \tag{A8}$$

and:

$$c_n = \sum_{k=0}^{n} \binom{n}{k} \left(\frac{\lambda_0}{1 - \lambda_0}\right)^k \tag{A9}$$

where $\binom{n}{k}$ are the binomial coefficients.

If we make the further assumption that λ_0 is much less than 1, Equation A7 becomes:

$$f_Z = \left(1 - (1 - \lambda_0)^n\right) \frac{n}{\alpha_0} e^{-nx/\alpha_0} \tag{A10}$$

which leads to:

$$\lambda = 1 - (1 - \lambda_0)^n \tag{A11}$$

and:

$$\alpha = \frac{\alpha_0 \lambda_0}{1 - (1 - \lambda_0)^n} \tag{A12}$$

Appendix B: TH-SPIM Implicit Algorithm Implementation

The procedure to update the height $h_{i,0}$ of a node at time t is as follows.

1. Obtain input parameters that are uniform in value: $K, m, n, \epsilon_c, p, b, \gamma, \Delta t, \Delta x$
2. Obtain input parameters that are specific to node i: μ_i, ν_i, A_i, h_r
3. Compute $F_1 = \frac{\Delta t K \mu_i^m A_i^m}{h_{i,0}} S_0^n$ and $F_2 = \frac{\Delta t \epsilon_c}{h_{i,0}} S_0^p$ where $S_0 = \frac{h_{i,0}}{\Delta x}$
4. Initialize $k = 0$ and $x_k = 1$
5. Compute $q_{c*} = \left(\frac{F_2}{F_1}\right)^{1/\gamma} x_k^{(p-n)/\gamma}$
6. Compute $\partial_x q_{c*} = q_{c*} \left(\frac{p-n}{\gamma}\right) x_k^{-1}$
7. Compute:
   - $\mu_\epsilon = \frac{\Gamma(1/\nu+\gamma)}{\Gamma(1/\nu)\nu^{-\gamma}} \Gamma(1/\nu + \gamma, q_{c*}/\nu)$ if $b = 1$
   - $\mu_\epsilon = \frac{\Gamma(1/\nu+1-\gamma)}{\Gamma(1/\nu)\nu^{\gamma-1}} \gamma(1/\nu + 1 - \gamma, 1/\nu q_{c*})$ if $b = 2$
   - $\lambda_\epsilon = \Gamma(1/\nu, q_{c*}/\nu)$ if $b = 1$
   - $\lambda_\epsilon = \gamma(1/\nu + 1, 1/\nu q_{c*})$ if $b = 2$
   - $\partial_{q_{c*}} \mu_\epsilon = -\frac{e^{-q_{c*}/\nu}(q_{c*}/\nu)^{1/\nu+\gamma-1}}{\Gamma(1/\nu)\nu^{-\gamma}}$ if $b = 1$
   - $\partial_{q_{c*}} \mu_\epsilon = -\frac{e^{-1/\nu q_{c*}}(1/\nu q_{c*})^{1/\nu-\gamma+2}}{\Gamma(1/\nu)\nu^{\gamma-2}}$ if $b = 2$
   - $\partial_{q_{c*}} \lambda_\epsilon = -\frac{e^{-q_{c*}/\nu}(q_{c*}/\nu)^{1/\nu-1}}{\Gamma(1/\nu)}$ if $b = 1$
   - $\partial_{q_{c*}} \lambda_\epsilon = -\frac{\nu e^{-1/\nu q_{c*}}(1/\nu q_{c*})^{1/\nu+2}}{\Gamma(1/\nu+1)}$ if $b = 2$
8. Compute $\partial_x \mu_\epsilon = \partial_{q_{c*}} \mu_\epsilon \partial_x q_{c*}$ and $\partial_x \lambda_\epsilon = \partial_{q_{c*}} \lambda_\epsilon \partial_x q_{c*}$
9. Compute $\bar{\mathcal{F}} = x - 1 + F_1 \mu_\epsilon x_k^n - F_2 \lambda_\epsilon x_k^p$

10. Compute $\partial_x \bar{\mathcal{F}} = 1 + F_1\left(\mu_\epsilon n x_k^{n-1} + \partial_x \mu_\epsilon x_k^n\right) - F_2\left(\lambda_\epsilon p x_k^{p-1} + \partial_x \lambda_\epsilon x_k^p\right)$

11. Compute $x_{k+1} = x_k - \frac{\bar{\mathcal{F}}}{\partial_x \bar{\mathcal{F}}}$ if $\bar{\mathcal{F}} > 0$ or $x_{k+1} = x_k$ otherwise

12. Check for convergence: if $\epsilon_k = |x_k - x_{k+1}| > tol$ set $k = k + 1$ and go back to 5; otherwise continue

13. Compute new height: $h_i = x_{k+1}(h_{i,0} - h_r) + h_r$

Appendix C: Newton-Raphson Convergence Criterion

If x_k is the estimate of the root x_r of function $\mathcal{F}(x)$ after k iterations, we can expand $\mathcal{F}(x_r)$ around x_k:

$$\mathcal{F}(x_r) = \mathcal{F}(x_k) + (x_r - x_k)\partial_x \mathcal{F}(x_k)(x_r - x_k) + \rho \tag{C1}$$

where ρ is the remainder of the expansion and can be expressed as:

$$\rho = \frac{1}{2}(x_r - x_k)^2 \partial_x^2 \mathcal{F}\left(x'\right) \tag{C2}$$

Because x_r is the root and thus $\mathcal{F}(x_r) = 0$, we can write:

$$(x_r - x_k) + \frac{\mathcal{F}(x_k)}{\partial_x \mathcal{F}(x_k)} = -(x_r - x_k)^2 \frac{1}{2}\frac{\partial_x^2 \mathcal{F}(x_k)}{\partial_x \mathcal{F}(x_k)} \tag{C3}$$

which leads to:

$$\epsilon_{k+1} = -\frac{1}{2}\frac{\partial_x^2 \mathcal{F}(x_k)}{\partial_x \mathcal{F}(x_k)}\epsilon_k \tag{C4}$$

as:

$$x_{k+1} = x_k - \frac{\mathcal{F}(x_k)}{\partial_x \mathcal{F}(x_k)} \tag{C5}$$

where $\epsilon_k = x_r - x_k$ and $\epsilon_{k+1} = x_r - x_{k+1}$ are the errors at iteration k and $k + 1$, respectively.

Equation C5 can also be expressed as:

$$|\epsilon_{k+1}| \leq L\epsilon_k^2 \tag{C6}$$

where:

$$L = \sup_{x \in [x_r, x_0]} \frac{1}{2}\left|\frac{\partial_x^2 \mathcal{F}(x_k)}{\partial_x \mathcal{F}(x_k)}\right| \tag{C7}$$

and shows that the Newton-Raphson scheme is quadratic, under the condition that:

$$L|\epsilon_0| < 1 \tag{C8}$$

Appendix D: $\mathcal{F}$ Second Derivative

The function for which a root must be found has the form:

$$\mathcal{F} = x - 1 + F_1 \mu_\epsilon(x)x^n - F_2 \lambda_e(x)x^p \tag{D1}$$

and to estimate the convergence criterion, we need to compute:

$$\partial_x^2 \mathcal{F} = F_1\left(\mu_\epsilon n(n-1)x^{n-2} + 2\partial_x \mu_\epsilon n x^{n-1} + \partial_x^2 \mu_\epsilon x^n\right) - F_2\left(\lambda_\epsilon p(p-1)x^{p-2} + 2\partial_x \lambda_\epsilon p x^{p-1} + \partial_x^2 \lambda_\epsilon x^p\right) \tag{D2}$$

with:

$$\partial_x^2 \mu_\epsilon = \partial_{q_{c*}}^2 \mu_\epsilon (\partial_x q_{c*})^2 + \partial_{q_{c*}} \mu_\epsilon \partial_x^2 q_{c*} \tag{D3}$$

and:

$$\partial_x^2 \lambda_\epsilon = \partial_{q_{c*}}^2 \lambda_\epsilon (\partial_x q_{c*})^2 + \partial_{q_{c*}} \lambda_\epsilon \partial_x^2 q_{c*} \tag{D4}$$

in which:

$$\partial_{q_{c*}}^2 \mu_\epsilon = e^{-q_{c*}/\nu} \frac{(q_{c*}/\nu)^{1/\nu+\gamma} - (1/\nu + \gamma - 1)(q_{c*}/\nu)^{1/\nu+\gamma-2}}{\Gamma(1/\nu)\nu^{-\gamma}} \quad \text{for } b = 1$$

$$\partial_{q_{c*}}^2 \mu_\epsilon = \frac{e^{-1/\nu q_{c*}}}{\Gamma(1/\nu + 1)\nu^{\gamma-3}} (1/\nu q_{c*})^{1/\nu-\gamma+3} \left[1/\nu - \gamma + 2 - (1/\nu q_{c*})^2\right] \quad \text{for } b = 2 \tag{D5}$$

and:

$$\partial_{q_{c*}}^2 \lambda_\epsilon = e^{-q_{c*}/\nu} \frac{(q_{c*}/\nu)^{1/\nu} - (1/\nu - 1)(q_{c*}/\nu)^{1/\nu-2}}{\Gamma(1/\nu)} \quad \text{for } b = 1$$

$$\partial_{q_{c*}}^2 \lambda_\epsilon = \frac{e^{-1/\nu q_{c*}}}{\Gamma(1/\nu + 1)\nu^{-2}} (1/\nu q_{c*})^{1/\nu+3} \left[1/\nu + 2 - (1/\nu q_{c*})^2\right] \quad \text{for } b = 2 \tag{D6}$$

and:

$$\partial_x^2 q_{c*} = q \left(\frac{p-n}{\gamma}\right) \left(\frac{p-n}{\gamma} - 1\right) x^{-2} \tag{D7}$$

We will now assume that the maximum value of $|\partial_{xx}\mathcal{F}/\partial_x\mathcal{F}|$ is reached when $x = 1$. We will call q_0 the critical discharge at $x = 1$ and from Equation 12, we can write:

$$q_0 = q_{c*}(x = 1) = \left(\frac{F_2}{F_1}\right)^{1/\gamma} \tag{D8}$$

and:

$$\partial_x q_{c*}(x = 1) = \partial_x q_0 = q_0 \left(\frac{p-n}{\gamma}\right) \text{and } \partial_x^2 q_{c*}(x = 1) = \partial_x^2 q_0 = q_0 \left(\frac{p-n}{\gamma}\right)\left(\frac{p-n}{\gamma} - 1\right) \tag{D9}$$

Finally, Equation D2 estimated at $x = 1$ becomes:

$$\partial_x^2\mathcal{F}(0) = F_1\left(\mu_{\epsilon,0}\, n(n-1) + 2\partial_x\mu_{\epsilon,0}\, n + \partial_x^2\mu_{\epsilon,0}\right) - F_2\left(\lambda_{\epsilon,0}\, p(p-1) + 2\partial_x\lambda_{\epsilon,0}\, p + \partial_x^2\lambda_{\epsilon,0}\right) \tag{D10}$$

with:

$$\mu_{\epsilon,0} = \mu_\epsilon(q_0) \text{ and } \lambda_{\epsilon,0} = \lambda_\epsilon(q_0)$$

$$\partial_x\mu_{\epsilon,0} = \partial_{q_{c*}}\mu_\epsilon(q_0)\, \partial_x q_0 \text{ and } \partial_x\lambda_{\epsilon,0} = \partial_{q_{c*}}\lambda_\epsilon(q_0)\, \partial_x q_0 \tag{D11}$$

$$\partial_x^2\mu_{\epsilon,0} = \partial_q^2\mu_\epsilon(q_0)(\partial_x q_0)^2 + \partial_{q_{c*}}\mu_\epsilon\partial_x^2 q_0 \text{ and } \partial_x^2\lambda_{\epsilon,0} = \partial_q^2\lambda_\epsilon(q_0)(\partial_x q_0)^2 + \partial_{q_{c*}}\lambda_\epsilon\partial_x^2 q_0$$

Appendix E: Erosional Decay Curve

During the erosional decay phase of a mountain belt, assuming that the SPIM controls the erosional process, topographic height, h, obeys the following partial differential equation:

$$\frac{\partial h}{\partial t} = -K A^m S^n \tag{E1}$$

Considering that during the decay phase the river network is frozen to the geometry that was set during the orogenic phase, one can hypothesize that, to first order, (a) the contributing drainage area is not going to evolve and is thus independent of time and (b) the slope is mostly dependent on the height, h and not on changes in horizontal length. We can therefore simplify this equation to be:

$$\frac{\partial H}{\partial t} = -K'H^n \tag{E2}$$

where H is a measure of mountain topographic height (mean or maximum). We can further simplify it using H', the mountain height normalized by its value at the end of the orogenic phase:

$$\frac{\partial H'}{\partial t} = -K'H'^n \tag{E3}$$

This equation has the following general solution:

$$H'(t) = \left[(n-1)\left(C + K't\right)\right]^{1/(n-1)} \tag{E4}$$

and knowing that $H'(t' = 0) = 1$ we can derive the value of the constant C to obtain:

$$H'(t) = \left[1 + (n-1)K't\right]^{1/(n-1)} \tag{E5}$$

By fitting the results of the numerical experiments shown in Figure 8a, we find that the optimum value of the parameter K' is π/τ where τ is the response time scale of the growth phase. This leads to:

$$H'(t) = [1 + (n-1)\pi t/\tau]^{1/(n-1)} \tag{E6}$$

Data Availability Statement

Data were not used, nor created for this research.

References

Ahnert, F. (1970). Functional relationships between denudation, relief, and uplift in large, mid-latitude drainage basins. *American Journal of Science*, *268*(3), 243–263. https://doi.org/10.2475/ajs.268.3.243

Baldwin, J. A., Whipple, K. X., & Tucker, G. E. (2003). Implications of the shear stress river incision model for the timescale of postorogenic decay of topography. *Journal of Geophysical Research*, *108*(B3), 2158. https://doi.org/10.1029/2001jb000550

Botter, G., Porporato, A., Rodriguez-Iturbe, I., & Rinaldo, A. (2007). Basin-scale soil moisture dynamics and the probabilistic characterization of carrier hydrologic flows: Slow, leaching-prone components of the hydrologic response. *Water Resources Research*, *43*(2), W02417. https://doi.org/10.1029/2006WR005043

Braun, J. (2023). *fastscape-lem/variablespim: Release 0.1.0*. Zenodo. https://doi.org/10.5281/zenodo.8233687

Braun, J., & Robert, X. (2005). Constraints on the rate of post-orogenic erosional decay from low-temperature thermochronological data: Application to the Dabie Shan, China. *Earth Surface Processes and Landforms*, *30*(9), 1203–1225. https://doi.org/10.1002/esp.1271

Braun, J., & Willett, S. D. (2013). A very efficient O(n), implicit and parallel method to solve the stream power equation governing fluvial incision and landscape evolution. *Geomorphology*, *180*, 170–179. https://doi.org/10.1016/j.geomorph.2012.10.008

Campforts, B., & Govers, G. (2015). Keeping the edge: A numerical method that avoids knickpoint smearing when solving the stream power law. *Journal of Geophysical Research: Earth Surface*, *120*(7), 1189–1205. https://doi.org/10.1002/2014JF003376

Curry, M. E., Beek, P. v. d., Huismans, R. S., Wolf, S. G., & Muñoz, J.-A. (2019). Evolving paleotopography and lithospheric flexure of the Pyrenean Orogen from 3D flexural modeling and basin analysis. *Earth and Planetary Science Letters*, *515*(37), 26–37. https://doi.org/10.1016/j.epsl.2019.03.009

Deal, E., Braun, J., & Botter, G. (2018). Understanding the role of rainfall and hydrology in determining fluvial erosion efficiency. *Journal of Geophysical Research: Earth Surface*, *123*(4), 744–778. https://doi.org/10.1002/2017JF004393

DiBiase, R. A., & Whipple, K. X. (2011). The influence of erosion thresholds and runoff variability on the relationships among topography, climate, and erosion rate. *Journal of Geophysical Research*, *116*(F4), F04036. https://doi.org/10.1029/2011JF002095

Doulatyari, B., Betterie, A., Radny, D., Celegon, E., Fanton, P., Schirmer, M., & Botter, G. (2017). Patterns of streamflow regimes along the river network: The case of the Thur River. *Environmental Modelling & Software*, *93*, 42–58. https://doi.org/10.1016/j.envsoft.2017.03.002

Egholm, D. L., Knudsen, M. F., & Sandiford, M. (2013). Lifespan of mountain ranges scaled by feedbacks between landsliding and erosion by rivers. *Nature*, *498*(7455), 475–478. https://doi.org/10.1038/nature12218

Hergarten, S. (2020). Transport-limited fluvial erosion – Simple formulation and efficient numerical treatment. *Earth Surface Dynamics*, *8*(4), 841–854. https://doi.org/10.5194/esurf-8-841-2020

Lague, D., Hovius, N., & Davy, P. (2005). Discharge, discharge variability, and the bedrock channel profile. *Journal of Geophysical Research*, *110*(F4), F04006. https://doi.org/10.1029/2004JF000259

Lamb, M. P., Dietrich, W. E., & Venditti, J. G. (2008). Is the critical Shields stress for incipient sediment motion dependent on channel-bed slope? *Journal of Geophysical Research*, *113*(F2), F02008. https://doi.org/10.1029/2007jf000831

Miller, M. C., McCave, I. N., & Komar, P. D. (1977). Threshold of sediment motion under unidirectional currents. *Sedimentology*, *24*(4), 507–527. https://doi.org/10.1111/j.1365-3091.1977.tb00136.x

Porporato, A., D'Odorico, P., Laio, F., Ridolfi, L., & Rodriguez-Iturbe, I. (2002). Ecohydrology of water-controlled ecosystems. *Advances in Water Resources*, *25*(8–12), 1335–1348. https://doi.org/10.1016/s0309-1708(02)00058-1

Royden, L., & Perron, J. (2013). Solutions of the stream power equation and application to the evolution of river longitudinal profiles. *Journal of Geophysical Research: Earth Surface*, *118*(2), 497–518. https://doi.org/10.1002/jgrf.20031

Scherler, D., DiBiase, R. A., Fisher, G. B., & Avouac, J. (2017a). Testing monsoonal controls on bedrock river incision in the Himalaya and Eastern Tibet with a stochastic-threshold stream power model. *Journal of Geophysical Research: Earth Surface*, *122*(7), 1389–1429. https://doi.org/10.1002/2016jf004011

Scherler, D., DiBiase, R. A., Fisher, G. B., & Avouac, J. (2017b). Testing monsoonal controls on bedrock river incision in the Himalaya and Eastern Tibet with a stochastic-threshold stream power model. *Journal of Geophysical Research: Earth Surface*, *122*(7), 1389–1429. https://doi.org/10.1002/2016jf004011

Snyder, N. P., Whipple, K. X., Tucker, G. E., & Merritts, D. J. (2003). Channel response to tectonic forcing: Field analysis of stream morphology and hydrology in the Mendocino triple junction region, northern California. *Geomorphology*, *53*(1–2), 97–127. https://doi.org/10.1016/s0169-555x(02)00349-5

Tucker, G., & Bras, R. (2000). A stochastic approach to modeling the role of rainfall variability in drainage basin evolution. *Water Resources Research*, *36*(7), 1953–1954. https://doi.org/10.1029/2000wr900065

von Blanckenburg, F. (2006). The control mechanisms of erosion and weathering at basin scale from cosmogenic nuclides in river sediment. *Earth and Planetary Science Letters*, *242*(3–4), 224–239. https://doi.org/10.1016/j.epsl.2005.11.017

Whipple, K., & Tucker, G. (1999). Dynamic of the Stream-Power river incision model: Implications for height limits of mountain ranges, landscape response timescales, and research needs. *Journal of Geophysical Research*, *104*(B8), 17661–17674. https://doi.org/10.1029/1999jb900120

Wolf, S. G., Huismans, R. S., Braun, J., & Yuan, X. (2022). Topography of mountain belts controlled by rheology and surface processes. *Nature*, *606*(7914), 516–521. https://doi.org/10.1038/s41586-022-04700-6